

**Jeong-Hoon Song**<sup>1</sup>  
Postdoctoral Fellow  
e-mail: j-song2@northwestern.edu

**Ted Belytschko**  
Walter P. Murphy Professor  
McCormick Professor

Theoretical and Applied Mechanics,  
Northwestern University,  
Evanston, IL 60208-3111

# Dynamic Fracture of Shells Subjected to Impulsive Loads

*A finite element method for the simulation of dynamic cracks in thin shells and its applications to quasibrittle fracture problem are presented. Discontinuities in the translational and angular velocity fields are introduced to model cracks by the extended finite element method. The proposed method is implemented for the Belytschko–Lin–Tsay shell element, which has high computational efficiency because of its use of a one-point integration scheme. Comparisons with elastoplastic crack propagation experiments involving quasibrittle fracture show that the method is able to reproduce experimental fracture patterns quite well. [DOI: 10.1115/1.3129711]*

## 1 Introduction

Simulation of fracture of shell structures is engendering considerable interest in the industrial and defense communities. Many components where fracture is of concern, such as windshields, ship hulls, fuel tanks, and car bodies, are not amenable to three dimensional solid modeling, for the expense would be enormous. Furthermore, fracture is often an important criterion in determining their performance envelopes.

Here, we describe a finite element method based on the extended finite element method (XFEM) [1,2] for modeling shell structures in explicit finite element programs and illustrate their performance in nonlinear problems involving dynamic fracture. The methodology is based on the Hansbo and Hansbo [3] approach, which has previously been applied by Mergheim et al. [4], Song et al. [5], and Areias et al. [6,7]. The equivalence of the Hansbo and Hansbo [3] basis functions to XFEM [1,2] is shown in Ref. [8]. The method employs an elementwise progression of the crack, i.e., the crack tip is always on an element edge. The elementwise crack propagation scheme may cause some noise during the crack propagation with coarse meshes. However, in Ref. [5], it is shown that such noise diminishes with mesh refinements and the crack propagation speeds converge to the progressive crack propagation results [9]. Réthoré et al. [10] reported that this is usually adequate for dynamic crack propagation. We do not use any near-tip enrichment, although Elguedj et al. [11] achieved good success with near-tip enrichments for static problems.

The literature in dynamic crack propagation in shells is quite limited. Cirak et al. [12] developed an interelement crack method, where the crack is limited to propagation along the element edges. The method is based on the Kirchhoff shell theory. Penalty functions were used to enforce continuity on all interelement edges. Areias and Belytschko [13] and Areias et al. [6,7] developed a method for shell fracture based on the extended finite element method for static and implicit time integrations.

The formulation described here also employs a cohesive law, but it requires a fracture criterion. As pointed out by Belytschko et al. [9], in models that inject a discontinuity in finite elements and in the governing partial differential equations, this appears to be a necessity, for a cohesive law is not sufficient to determine a direction or a speed of crack propagation. In the interelement crack methods, such as Cirak et al. [12], a fracture criterion is avoided by injecting cohesive laws either from the beginning of the simu-

lation or in the vicinity of the crack tip [14]. In related work, Armero and Ehrlich [15] used embedded discontinuity elements to model hinge lines in plates.

The development of a fracture criterion that is computationally efficient and is easily applied in terms of available data poses a significant difficulty. Fracture criteria for quasibrittle materials, such as aluminum, are usually expressed in terms of the critical maximum principal tensile strain. However, in low order finite element models solved by explicit time integration, the maximum principal tensile strain tends to be quite noisy, so that crack paths computed by direct application of such a criterion tend to be erratic and do not conform to experimentally observed crack paths.

Here, we propose a nonlocal form of a strain-based fracture criterion. The nonlocal form is obtained by a kernel-weighted average over a sector in front of the crack tip. In addition, we describe a combination of this kernel-weighted average with an angular component that can be used to indicate crack branching.

The methodology is applied to the fracture of shell experiments performed by Chao and Shepherd [16]. Although these experiments are very interesting, they do not provide enough experimental data for a validation of the methodology. Nevertheless, we show that the method is able to reproduce the change in failure mode that occurs for longer notches as compared with shorter notches and that the overall final configuration agrees reasonably well with that observed in the experiments.

## 2 Shell Formulation With Fracture

The discontinuous shell formulation is based on the degenerated shell concept [17–19], which is almost equivalent to the Mindlin–Reissner formulation when the edges connecting the top and bottom surfaces are normal to the midsurface. We will use a kinematic theory based on the corotational rate-of-deformation and corotational Cauchy stress rate. These features are briefly summarized in Sec. 3, but are well known, so we will focus on the modifications needed for the XFEM treatment of fracture.

The velocity field is given by

$$\mathbf{v}(\boldsymbol{\xi}, t) = \mathbf{v}^{\text{mid}}(\boldsymbol{\xi}, t) - \zeta \mathbf{e}_3 \times \boldsymbol{\theta}^{\text{mid}}(\boldsymbol{\xi}, t) \quad (1)$$

where  $\mathbf{v}^{\text{mid}} \in \mathcal{R}^3$  are the velocities of the shell midsurface,  $\boldsymbol{\theta}^{\text{mid}} \in \mathcal{R}^3$  are angular velocities of the normals to the midsurface,  $\zeta$  varies linearly from  $-h/2$  to  $h/2$  along the thickness, and  $\boldsymbol{\xi} = (\xi_1, \xi_2)$  are material coordinates of the manifold that describes the midsurface of the shell; at any point of the shell, we construct tangent unit vectors  $\mathbf{e}_1$  and  $\mathbf{e}_2$  so that

$$\mathbf{e}_3 = \mathbf{e}_1 \times \mathbf{e}_2 \quad (2)$$

The nomenclature is illustrated in Fig. 1.

For the further development of the discontinuous shell formulation, we will limit ourselves to cracks with surfaces normal to

<sup>1</sup>Corresponding author.

Contributed by the Applied Mechanics Division of ASME for publication in the JOURNAL OF APPLIED MECHANICS. Manuscript received November 30, 2007; final manuscript received September 16, 2008; published online June 12, 2009. Review conducted by Ashkan Vaziri.

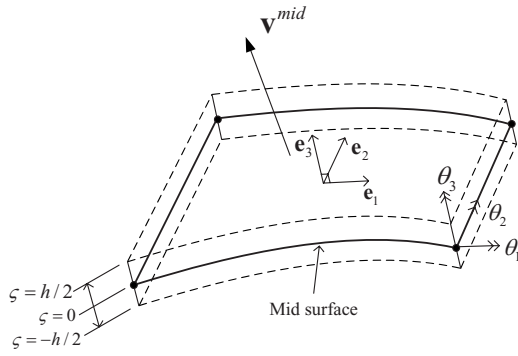


Fig. 1 The nomenclature of a continuum shell description

the shell midsurfaces as shown in Fig. 2. Although this is not an intrinsic limitation of the method, it simplifies several aspects of the formulation.

The discontinuous velocity fields due to a crack in any Mindlin–Reissner theory can be described by

$$\mathbf{v}^{\text{mid}}(\boldsymbol{\xi}, t) = \mathbf{v}^{\text{cont}}(\boldsymbol{\xi}, t) + H(f(\boldsymbol{\xi}))\mathbf{v}^{\text{disc}}(\boldsymbol{\xi}, t) \quad (3)$$

$$\boldsymbol{\theta}^{\text{mid}}(\boldsymbol{\xi}, t) = \boldsymbol{\theta}^{\text{cont}}(\boldsymbol{\xi}, t) + H(f(\boldsymbol{\xi}))\boldsymbol{\theta}^{\text{disc}}(\boldsymbol{\xi}, t) \quad (4)$$

where  $f(\boldsymbol{\xi})=0$  gives the intersection of the crack surface with the midsurface of the shell and  $H(\cdot)$  is the Heaviside function given by

$$H(x) = \begin{cases} 1, & x > 0 \\ 0, & x \leq 0 \end{cases} \quad (5)$$

In the above,  $\mathbf{v}^{\text{cont}}$  and  $\mathbf{v}^{\text{disc}}$  are continuous functions that are used to model the continuous and the discontinuous parts of the velocity fields, respectively; similarly,  $\boldsymbol{\theta}^{\text{cont}}$  and  $\boldsymbol{\theta}^{\text{disc}}$  are continuous functions. The discontinuities that model the cracks arise from the step function that precedes  $\mathbf{v}^{\text{disc}}$  and  $\boldsymbol{\theta}^{\text{disc}}$ . It can be seen from Eqs. (3) and (4) with Eq. (1) that these velocity fields can result in a loss of compatibility and, in particular, material overlaps in the displacements, as indicated in Fig. 3, when there are significant discontinuities in the angular motion but the crack opening is small. We will deal this incompatibility with a penalty component in the cohesive law; see Sec. 4.

### 3 Element Formulation

The shell element used here is a four-node shell element originally described in Ref. [20] with improvements in Refs. [5,21]. The shell element employs a one-point quadrature rule with stabilization [22,23] for computational efficiency.

When the velocity fields given in Eqs. (3) and (4) are specialized to shell finite elements, the continuous part of the corotational velocity components is given by

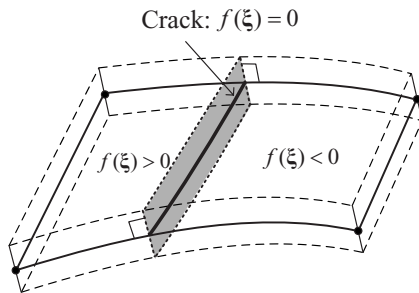


Fig. 2 Representation of discontinuity in the reference configuration by a level set implicit function  $f(\boldsymbol{\xi})$  in the shell midsurface

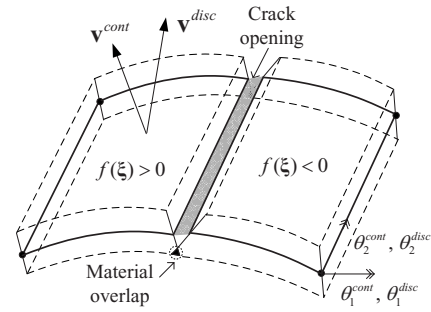


Fig. 3 Nomenclature of a fractured shell descriptions: incompatible material overlaps occurred at the bottom surface due to crack opening

$$\hat{v}_x(\boldsymbol{\xi}, t) = N_I(\boldsymbol{\xi})\hat{v}_{xI}(t) + \zeta N_I(\boldsymbol{\xi})\hat{\theta}_{xI}(t) \quad (6)$$

$$\hat{v}_y(\boldsymbol{\xi}, t) = N_I(\boldsymbol{\xi})\hat{v}_{yI}(t) - \zeta N_I(\boldsymbol{\xi})\hat{\theta}_{yI}(t) \quad (7)$$

where  $N_I$  are the conventional four-node finite element bilinear shape functions and the repeated subscripts  $I$  denote summation over all nodes. The corotational components of the rate-of-deformation tensor are given by

$$\hat{D}_{ij} = \frac{1}{2} \left( \frac{\partial \hat{v}_i}{\partial \hat{x}_j} + \frac{\partial \hat{v}_j}{\partial \hat{x}_i} \right) \quad (8)$$

Substituting Eqs. (6) and (7) into Eq. (8) yields an expression for the rate-of-deformation components

$$\hat{D}_x = \mathbf{b}_{xI}\hat{v}_{xI} + \zeta(\mathbf{b}_{xI}^c\mathbf{v}_{xI} + \mathbf{b}_{xI}\boldsymbol{\theta}_{yI}) \quad (9)$$

$$\hat{D}_y = \mathbf{b}_{yI}\hat{v}_{yI} + \zeta(\mathbf{b}_{yI}^c\mathbf{v}_{yI} - \mathbf{b}_{yI}\boldsymbol{\theta}_{xI}) \quad (10)$$

$$2\hat{D}_{xy} = \mathbf{b}_{xI}\hat{v}_{yI} + \mathbf{b}_{yI}\hat{v}_{xI} + \zeta(\mathbf{b}_{xI}^c\mathbf{v}_{yI} + \mathbf{b}_{yI}^c\mathbf{v}_{xI} + \mathbf{b}_{xI}\boldsymbol{\theta}_{yI} - \mathbf{b}_{yI}\boldsymbol{\theta}_{xI}) \quad (11)$$

where

$$\begin{Bmatrix} \mathbf{b}_{xI} \\ \mathbf{b}_{yI} \end{Bmatrix} = \frac{1}{2A} \begin{bmatrix} \hat{y}_{24} & \hat{y}_{31} & \hat{y}_{42} & \hat{y}_{13} \\ \hat{x}_{42} & \hat{x}_{13} & \hat{x}_{24} & \hat{x}_{31} \end{bmatrix} \quad (12)$$

$$\begin{Bmatrix} \mathbf{b}_{xI}^c \\ \mathbf{b}_{yI}^c \end{Bmatrix} = \frac{2\hat{\gamma}_K\hat{z}_K}{A^2} \begin{bmatrix} \hat{x}_{13} & \hat{x}_{42} & \hat{x}_{31} & \hat{x}_{24} \\ \hat{y}_{13} & \hat{y}_{42} & \hat{y}_{31} & \hat{y}_{24} \end{bmatrix} \quad (13)$$

along with  $\hat{x}_{IJ} = \hat{x}_I - \hat{x}_J$ ,  $A$  is the area of the element, and  $\hat{\gamma}_K$  is a projection operator: See Ref. [22]. A state of plane stress is assumed. In Ref. [21], two methods are proposed for the evaluation of  $\mathbf{b}^c$ . Here in Eq. (13), we adopted the  $\hat{z}$  method. In this case, curvature is only coupled with the translations for a warped element.

We also used the shear projection scheme introduced in Ref. [21]. This shear projection scheme gives the transverse shear strain components by

$$\hat{D}_{xz} = \mathbf{b}_{x1I}^s\hat{v}_{zI} + \mathbf{b}_{x2I}^s\hat{\theta}_{xI} + \mathbf{b}_{x3I}^s\hat{\theta}_{yI} \quad (14)$$

$$\hat{D}_{yz} = \mathbf{b}_{y1I}^s\hat{v}_{zI} + \mathbf{b}_{y2I}^s\hat{\theta}_{xI} + \mathbf{b}_{y3I}^s\hat{\theta}_{yI} \quad (15)$$

where

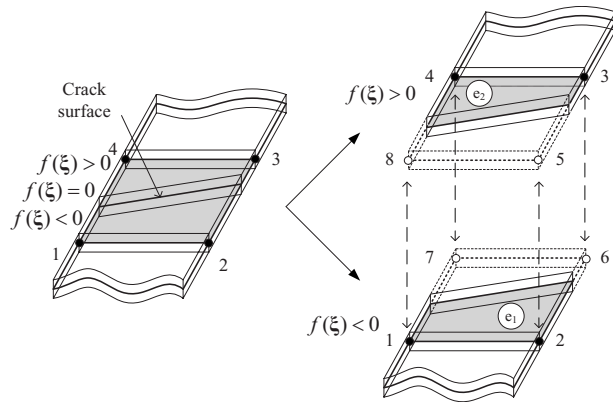


**Fig. 4** The decomposition of a cracked element with generic nodes 1–4 into two elements  $e_1$  and  $e_2$ ; solid and hollow circles denote the original nodes and the added phantom nodes, respectively

$$\begin{Bmatrix} \mathbf{b}_{x1I}^s & \mathbf{b}_{x2I}^s & \mathbf{b}_{x3I}^s \\ \mathbf{b}_{y1I}^s & \mathbf{b}_{y2I}^s & \mathbf{b}_{y3I}^s \end{Bmatrix} = \frac{1}{4} \begin{bmatrix} 2(\bar{x}_{JI} - \bar{x}_{IK}) & (\hat{x}_{JI}\bar{y}_{JI} + \hat{x}_{IK}\bar{y}_{IK}) & -(\hat{x}_{JI}\bar{y}_{JI} + \hat{x}_{IK}\bar{y}_{IK}) \\ 2(\bar{y}_{JI} - \bar{y}_{IK}) & (\hat{y}_{JI}\bar{y}_{JI} + \hat{y}_{IK}\bar{y}_{IK}) & -(\hat{y}_{JI}\bar{y}_{JI} + \hat{y}_{IK}\bar{y}_{IK}) \end{bmatrix} \quad (16)$$

along with  $(I, J, K) = \{(I, J, K) | (1, 2, 4), (2, 3, 1), (3, 4, 1), (4, 1, 3)\}$  and  $\bar{x}_{IJ} = \hat{x}_{IJ} / \|\hat{x}_{IJ}\|$ .

**3.1 Representation of the Discontinuity.** The velocity field of the fractured shell element, which is given by Eqs. (3) and (4), can be approximated in the XFEM by

$$\hat{\mathbf{v}}^{\text{mid}}(\boldsymbol{\xi}, t) = N_I(\boldsymbol{\xi})\hat{\mathbf{v}}_I^{\text{cont}}(t) + H(f(\boldsymbol{\xi}))N_I(\boldsymbol{\xi})\hat{\mathbf{v}}_I^{\text{disc}}(t) \quad (17)$$

$$\hat{\boldsymbol{\theta}}^{\text{mid}}(\boldsymbol{\xi}, t) = N_I(\boldsymbol{\xi})\hat{\boldsymbol{\theta}}_I^{\text{cont}}(t) + H(f(\boldsymbol{\xi}))N_I(\boldsymbol{\xi})\hat{\boldsymbol{\theta}}_I^{\text{disc}}(t) \quad (18)$$

However, when elementwise crack propagation is employed, we have found that it is simpler to program the implementation in the Hansbo and Hansbo [3] form, as developed by Song et al. [5]. The element completely cut by a crack is represented by a set of overlapping elements with added phantom nodes as shown in Fig. 4.

The discontinuous velocity field is then constructed by two superimposed velocity fields

$$\begin{aligned} \hat{\mathbf{v}}(\boldsymbol{\xi}, t) &= \hat{\mathbf{v}}^{e_1}(\boldsymbol{\xi}, t) + \hat{\mathbf{v}}^{e_2}(\boldsymbol{\xi}, t) = \sum_{I \in S_1} N_I(\boldsymbol{\xi})H(-f(\boldsymbol{\xi}))\hat{\mathbf{v}}_I^{e_1}(t) \\ &+ \sum_{I \in S_2} N_I(\boldsymbol{\xi})H(f(\boldsymbol{\xi}))\hat{\mathbf{v}}_I^{e_2}(t) \end{aligned} \quad (19)$$

$$\begin{aligned} \hat{\boldsymbol{\theta}}(\boldsymbol{\xi}, t) &= \hat{\boldsymbol{\theta}}^{e_1}(\boldsymbol{\xi}, t) + \hat{\boldsymbol{\theta}}^{e_2}(\boldsymbol{\xi}, t) = \sum_{I \in S_1} N_I(\boldsymbol{\xi})H(-f(\boldsymbol{\xi}))\hat{\boldsymbol{\theta}}_I^{e_1}(t) \\ &+ \sum_{I \in S_2} N_I(\boldsymbol{\xi})H(f(\boldsymbol{\xi}))\hat{\boldsymbol{\theta}}_I^{e_2}(t) \end{aligned} \quad (20)$$

where  $S_1$  and  $S_2$  are the sets of the nodes of the overlapping elements  $e_1$  and  $e_2$ , respectively. Note that velocity fields  $\hat{\mathbf{v}}^{e_1}(\boldsymbol{\xi}, t)$  and  $\hat{\mathbf{v}}^{e_2}(\boldsymbol{\xi}, t)$  (or  $\hat{\boldsymbol{\theta}}^{e_1}(\boldsymbol{\xi}, t)$  and  $\hat{\boldsymbol{\theta}}^{e_2}(\boldsymbol{\xi}, t)$ ) are nonzero only for  $f(\boldsymbol{\xi}) < 0$  and  $f(\boldsymbol{\xi}) > 0$ , respectively, due to the Heaviside step function  $H(x)$  that appears in the above equations. The phantom nodes are integrated in time by the same central difference explicit method as the remaining nodes.

**3.2 Representation of Multiple Discontinuities: Crack Branching.** The concept of the overlapping element method can be easily extended to crack branch modeling. When the original

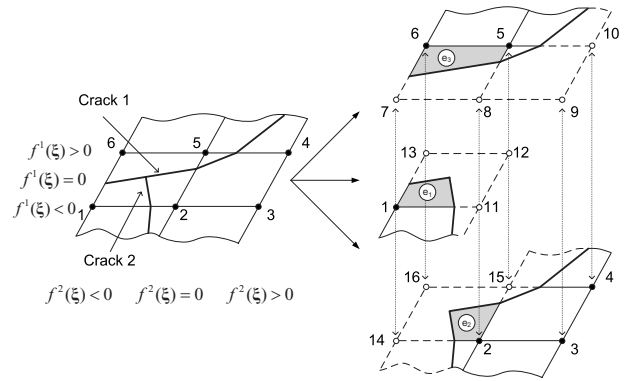


**Fig. 5** The decomposition of an element into three elements  $e_1$ ,  $e_2$ , and  $e_3$  to model crack branching; solid and hollow circles denote the original nodes and the added phantom nodes, respectively

crack, crack 1, branches into crack 1 and crack 2, as shown in Fig. 5, the element in which the crack branches is replaced with three overlapping elements. Let  $f^1(\boldsymbol{\xi})=0$  describe the original crack and one branch, and let  $f^2(\boldsymbol{\xi})=0$  describe the second branch. The discontinuous velocity field is then given by

$$\begin{aligned} \hat{\mathbf{v}}(\boldsymbol{\xi}, t) &= \hat{\mathbf{v}}^{e_1}(\boldsymbol{\xi}, t) + \hat{\mathbf{v}}^{e_2}(\boldsymbol{\xi}, t) + \hat{\mathbf{v}}^{e_3}(\boldsymbol{\xi}, t) \\ &= \sum_{I \in S_1} N_I(\boldsymbol{\xi})H(-f^1(\boldsymbol{\xi}))H(-f^2(\boldsymbol{\xi}))\hat{\mathbf{v}}_I^{e_1}(t) \\ &+ \sum_{I \in S_2} N_I(\boldsymbol{\xi})H(-f^1(\boldsymbol{\xi}))H(f^2(\boldsymbol{\xi}))\hat{\mathbf{v}}_I^{e_2}(t) \\ &+ \sum_{I \in S_3} N_I(\boldsymbol{\xi})H(f^1(\boldsymbol{\xi}))H(-f^2(\boldsymbol{\xi}))\hat{\mathbf{v}}_I^{e_3}(t) \end{aligned} \quad (21)$$

The element nodal forces are developed as in Ref. [20]. In addition, curvature-translation coupling terms are added and a shear projection operator replaces the previous transverse shear terms. The principle of virtual power is used to derive the relationship for the internal nodal forces. The principle states that

$$\begin{aligned} \delta \mathcal{P}^{\text{int}} &= \underbrace{A(\mathbf{B}_m \delta \mathbf{v})^T \begin{Bmatrix} \hat{f}_x^r \\ \hat{f}_y^r \\ \hat{f}_{xy}^r \end{Bmatrix}}_{\text{virtual membrane power}} + \underbrace{A(\mathbf{B}_b \delta \mathbf{v})^T \begin{Bmatrix} \hat{m}_x^r \\ \hat{m}_y^r \\ \hat{m}_{xy}^r \end{Bmatrix}}_{\text{virtual bending power}} \\ &+ \underbrace{\bar{\kappa} A(\mathbf{B}_s \delta \mathbf{v})^T \begin{Bmatrix} \hat{f}_{xz}^r \\ \hat{f}_{yz}^r \end{Bmatrix}}_{\text{virtual transverse shear power}} \end{aligned} \quad (22)$$

where  $\bar{\kappa}$  is the shear reduction factor from the Mindlin shell theory, and  $\hat{f}_{ij}^r$  and  $\hat{m}_{ij}^r$  are the resultant forces and moments, which are integrated through the element thickness.

$$\hat{f}_{ij}^r = \int \hat{\sigma}_{ij} d\hat{z} \quad (23)$$

$$\hat{m}_{ij}^r = \int \hat{z} \hat{\sigma}_{ij} d\hat{z} \quad (24)$$

where  $\hat{z} = \zeta(h/2)$ .

We substitute Eqs. (9)–(16) into Eq. (22), and evoking the arbitrariness of  $\delta \mathbf{v}$  yields the discretized element nodal forces

$$\hat{f}_{xI}^{\text{int}} = A_e(b_{xI}\hat{f}_x^r + b_{yI}\hat{f}_{xy}^r + b_{xI}^c\hat{m}_x^r + b_{yI}^c\hat{m}_{xy}^r) \quad (25)$$

$$\hat{f}_{yI}^{\text{int}} = A_e(b_{yI}\hat{f}_y^r + b_{xI}\hat{f}_{xy}^r + b_{yI}^c\hat{m}_y^r + b_{xI}^c\hat{m}_{xy}^r) \quad (26)$$

$$\hat{f}_{zI}^{\text{int}} = A_e\bar{\kappa}(b_{xI}\hat{f}_{xz}^r + b_{yI}\hat{f}_{yz}^r) \quad (27)$$

$$\hat{m}_{xI}^{\text{int}} = A_e[\bar{\kappa}(b_{x2I}\hat{f}_{xz}^r + b_{y2I}\hat{f}_{yz}^r) - (b_{yI}\hat{m}_y^r + b_{xI}\hat{m}_{xy}^r)] \quad (28)$$

$$\hat{m}_{yI}^{\text{int}} = A_e[\bar{\kappa}(b_{x3I}\hat{f}_{xz}^r + b_{y3I}\hat{f}_{yz}^r) + (b_{xI}\hat{m}_x^r + b_{yI}\hat{m}_{xy}^r)] \quad (29)$$

$$\hat{m}_{zI}^{\text{int}} = 0 \quad (30)$$

The final form of the element internal forces in the global coordinates can be determined by performing the transformation between the corotational and global coordinates as follows:

$$\mathbf{f}_e^{\text{int}} = \mathbf{T}_e^T(\hat{\mathbf{f}}_e^{\text{int}} + \hat{\mathbf{f}}_e^{\text{stab}}) \quad (31)$$

where  $\mathbf{T}$  is the transformation matrix between global and corotational components and  $\hat{\mathbf{f}}_e^{\text{int}}$  is the nodal internal force vector in the corotational coordinate systems. In Eq. (31), to circumvent the rank deficiency due to one-point integration, an hourglass control force,  $\hat{\mathbf{f}}_e^{\text{stab}}$ , is added to the internal force vector. For a description of the hourglass control scheme, see Refs. [21,22].

For each of the overlapped elements on a crack, the nodal forces are given by

$$\mathbf{f}_e^{\text{int}} = \left( \sum_{k=1}^{N_{\text{ele}}^{\text{ovr}}} \frac{A_{e_k}}{A_e} \mathbf{T}_{e_k}^T \hat{\mathbf{f}}_{e_k}^{\text{int}} \right) + \mathbf{T}_e^T \hat{\mathbf{f}}_e^{\text{stab}} \quad (32)$$

where  $N_{\text{ele}}^{\text{ovr}}$  is the total number of overlapped elements,  $A_{e_k}$  is the activated area of the corresponding overlapping elements in the corotational coordinates,  $\mathbf{f}_e$  is the nodal force vector of a cracked element, and  $\hat{\mathbf{f}}_{e_k}$  is the corotational nodal force vector of the overlapped element  $e_k$ . Note that the internal nodal forces of elements  $e_k$  can be calculated by multiplying Eqs. (25)–(30) by the area fraction,  $A_{e_k}/A_e$ . A more detailed discussion of the concept of the modification of cracked element nodal forces by area fractions can be found in Ref. [5].

## 4 Material Model and Fracture

**4.1 Hardening Plasticity for Quasibrittle Material.** We employed a von Mises type hardening  $J_2$ -plasticity model. For the integration of the constitutive model we used a first-order forward Euler explicit integration scheme. In the simulation of fracture within the explicit simulation framework, the integration time step is limited to a small fraction of the critical time step and is usually smaller than a critical time step for the integration of the constitutive equation.

The rate form of the constitutive equation in the corotational system is given by

$$\frac{D\hat{\boldsymbol{\sigma}}}{Dt} = \hat{\mathbf{C}}^{\text{elas}} : (\hat{\mathbf{D}} - \hat{\mathbf{D}}^p) \quad (33)$$

where  $\hat{\boldsymbol{\sigma}}$  is the corotational Cauchy stress rate,  $\hat{\mathbf{C}}^{\text{elas}}$  is the corotational elastic moduli tensor, and  $\hat{\mathbf{D}}^p$  is the corotational rate of plastic deformation tensor. For the von Mises material with isotropic hardening, the plastic corotational rate-of-deformation tensor is given by

$$\hat{\mathbf{D}}^p = \mathbf{r} \dot{\lambda} = \mathbf{r} \frac{\mathbf{r} : \hat{\mathbf{C}}^{\text{elas}} : \hat{\mathbf{D}}}{\mathbf{r} : \hat{\mathbf{C}}^{\text{elas}} : \mathbf{r} + h_p} \quad (34)$$

where  $\mathbf{r}$  is  $J_2$ -plasticity flow direction,  $\dot{\lambda}$  is plastic flow rate parameter, and  $h_p$  is the plastic hardening modulus.

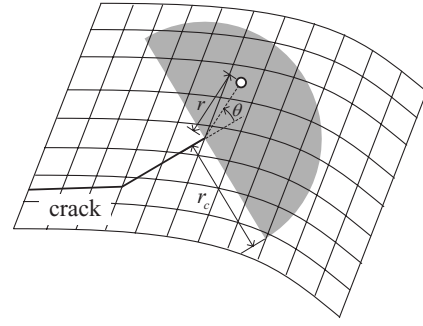


Fig. 6 Schematic of averaging domain: averaging domain, which has averaging size of  $r_c$

**4.2 Fracture Criterion and Cohesive Model.** A strain-based fracture criterion was used to determine the onset point of a post-strain localization behavior of a material, i.e., fracture. When the strain at a crack tip material point reaches a fracture threshold, we inject a strong discontinuity at the previous crack tip according to maximum principal tensile strain direction of an averaged strain,  $\epsilon^{\text{avg}}$ . For the computation of an averaged strain,  $\epsilon^{\text{avg}}$ , we used a nonlocal (i.e., surface weighted average) scheme, which is given by

$$\epsilon^{\text{avg}} = \frac{4}{\pi} \int_{-\pi/2}^{\pi/2} \int_0^{r_c} w(r) \epsilon \, r \, d\theta \quad (35)$$

where  $r$  and  $\theta$  are the distance from the crack tip and the angle with the tangent to the crack path, respectively, and  $w(r)$  is weight function; for the latter, we use a cubic spline function given by

$$w(r) = \begin{cases} 4 \left( \frac{r}{r_c} - 1 \right) \left( \frac{r}{r_c} \right)^2 + \frac{2}{3}, & 0 < r < 0.5r_c \\ \frac{4}{3} \left( 1 - \frac{r}{r_c} \right)^3, & 0.5r_c \leq r \leq r_c \\ 0 & \text{otherwise} \end{cases} \quad (36)$$

where  $r_c (\approx 3h_e)$  is the size of the averaging domain, and  $h_e$  is the size of the crack tip element. A typical averaging domain is shown in Fig. 6.

A cohesive crack model is prescribed along the newly injected strong discontinuity surfaces until the crack opening is fully developed, i.e., cohesive traction has vanished. In this study, we prescribed only the normal traction of the linear cohesive model, as shown in Fig. 7. We have found that mode II and mode III

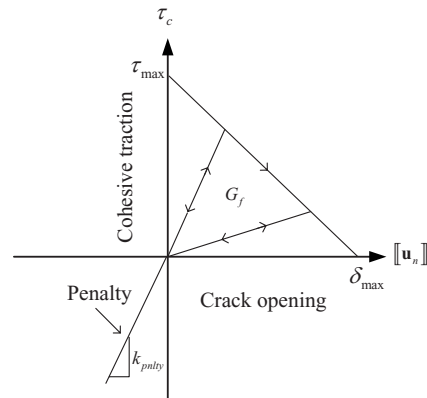
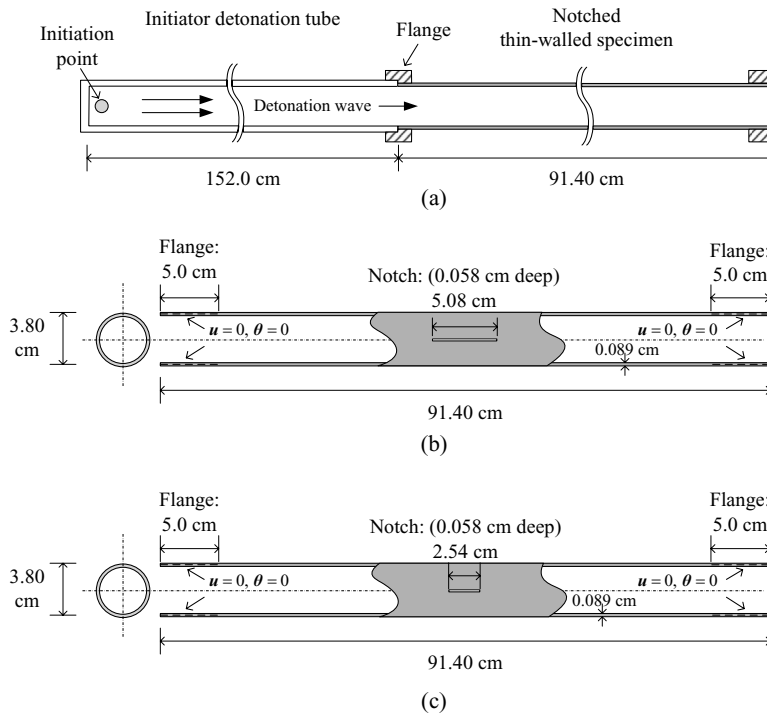


Fig. 7 Schematic showing of a linear cohesive law: the area under curve is the fracture energy,  $G_f$



**Fig. 8 Setup for the notched cylinder fracture under internal detonation pressure [16]: (a) total experiment assembly, (b) notched thin-walled specimen for shot 7, and (c) notched thin-walled specimen for shot 4**

behavior is minimal in these problems, perhaps because fracture occurs in a tearing mode.

The cohesive model is constructed so that the dissipated energy due to the crack propagation is equivalent to the fracture energy

$$G_f = \int_0^{\delta_{\max}} \tau_c(\delta_n) d\delta = \frac{1}{2} \tau_{\max} \delta_{\max} \quad (37)$$

where  $\delta_{\max}$  is the maximum crack opening displacement,  $G_f$  is the fracture energy, and  $\delta_n$  is the jump in the displacement normal to the crack surface,  $\Gamma_d$ , which is given by

$$\delta_n = \mathbf{n} \cdot [\mathbf{u}(\boldsymbol{\xi}, t)]_{\boldsymbol{\xi} \in \Gamma_d} \quad (38)$$

$$= \mathbf{n} \cdot [N_j(\boldsymbol{\xi}) \mathbf{u}_j^{e_2}(t) - N_j(\boldsymbol{\xi}) \mathbf{u}_j^{e_1}(t)]_{\boldsymbol{\xi} \in \Gamma_d} \quad (39)$$

where  $\mathbf{n}$  is the normal to the crack surface. Note that the cohesive strength  $\tau_{\max}$  is not a constant parameter in this method. Unless  $\tau_{\max}$  takes on the current value of the traction when a crack segment is injected into a continuum finite element, the cohesive traction does not satisfy time continuity and may lead to severe noise; see Ref. [24].

As shown in Fig. 7, a penalty force was added in compression. This penalty force depends only on  $\delta_n$  and is given by  $\tau_c = \delta_n k_{\text{pnltly}}$  when  $\delta_n < 0$ . We used a value of two to three orders of magnitudes of the normalized Young's modulus by the element size, i.e.,  $E/h_e$ , for  $k_{\text{pnltly}}$ .

The discretized form of the cohesive nodal forces is computed by

$$\mathbf{f}_e^{\text{coh}} = \sum_{k=1}^2 \mathbf{T}_{e_k}^T \hat{\mathbf{f}}_{e_k}^{\text{coh}} \quad (40)$$

$$= \sum_{k=1}^2 \mathbf{T}_{e_k}^T (-1)^k \int_{\Gamma_d} \mathbf{N}^T \tau_c(\delta_n) \hat{\mathbf{n}} d\Gamma_d \quad (41)$$

where  $k$  represents the overlaid element layer number.

## 5 Numerical Examples

### 5.1 Notched Cylinder Fracture Under Internal Detonation Pressure.

An interesting series of experiments concerned with the quasibrittle fracture of shells has been reported by Chao and Shepherd [16], and Chao [25]. These experiments involve notched thin-wall pipes filled with gaseous explosives through which a detonation wave is passed. This is accomplished in the experiment by filling the pipe with an explosive gas and initiating a detonation wave at the left end as shown in Fig. 8(a).

In this study, we focused on numerical simulations of two experimental results, shot 7 ( $L=5.08$  cm) and shot 4 ( $L=2.54$  cm) [16,25], since these two experimental results exhibit strikingly different growths of the fracture, which is ascribed to the length of the notch. Chao and Shepherd [16], and Chao [25] reported that with a notch size of  $L=5.08$  cm, the *backward* crack tip, which is closer to the detonation initiation point, showed a curving crack path, whereas the *forward* crack tip propagates only a short distance in a straight line and then bifurcated into two cracks. However, with a notch size of  $L=2.54$  cm, the backward crack tip curved, whereas the forward crack tip propagates only a short distance in a straight line and then is arrested.

For the numerical simulation, we discretized the right segment of the cylinder length of the 91.40 cm with 54,382 four-node quadrilateral shell elements ( $h_e \approx 0.90$  mm); see Figs. 8(b) and 8(c). The shell material is aluminum 6061-T6 and we modeled it with  $J_2$ -plasticity, density  $\rho=2780.0$  kg/m<sup>3</sup>, Young's modulus  $E=69.0$  GPa, Poisson's ratio  $\nu=0.30$ , and yield stress  $\sigma_y=275.0$  MPa. We used linear hardening with constant slope  $h_p=640.0$  MPa. The cohesive fracture energy  $G_f=19.0$  kJ/m<sup>2</sup> is treated in terms of a cohesive law (the assigned fracture energy is based on Refs. [26–28]).

In order to induce unsymmetrical crack propagation with an axisymmetric shell structure and loading, we introduced a small scatter in the yield strength of bulk material. The yield strength at every material point is perturbed by factors ranging from  $-5.0\%$  to  $5.0\%$ : The perturbation factor is obtained from a log-normal

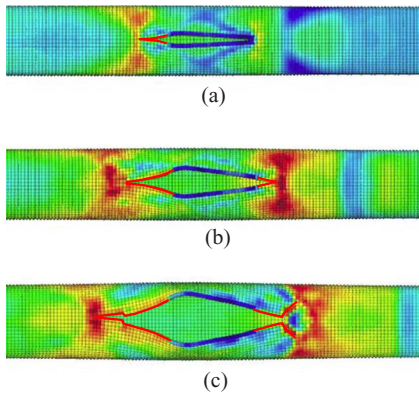


**Fig. 9 Evolution of crack paths and distributions of effective plastic stress at different time steps: (a)  $t=213.55 \mu\text{s}$ , (b)  $t=228.61 \mu\text{s}$ , and (c)  $t=238.01 \mu\text{s}$ . Note that finite element nodes are plotted and crack paths are explicitly marked.**

distribution around the mean value of 1.0 and a standard deviation of 2.0%. We also considered bulk materials in which the yield strength is perturbed by  $\pm 10.0\%$ ; the results are almost identical.

For the fracture criterion, we used 6% maximum tensile strain as the fracture strain. This strain value was used to nucleate any new cracks and to propagate cracks, but in these simulations no new crack were nucleated as the notches and subsequent cracks served as the only nucleation mechanism. The cracks were propagated in the direction normal to the direction of maximum principal strain.

For the applied pressure, we used a pressure time history function,  $p(x, t)$ , which is provided by Beltman and Shepherd [29] as follows:

$$p(x, t) = \begin{cases} 0, & t < x/v^{cj} \\ p^{cj} \exp(-(t - x/v^{cj})/T_0), & t > x/v^{cj} \end{cases} \quad (42)$$

where  $x$  is the axial distance from the detonation initiation source to the material point,  $t$  is the simulation time,  $T_0 (\approx 3.0x/v^{cj})$  is pressure decay time, and  $p^{cj}$  and  $v^{cj}$  are the Chapmand–Jouguet pressure and detonation wave propagation velocity, respectively. For the simulation, we used  $p^{cj}=6.2$  MPa and  $v^{cj}=2390$  m/s to model the internal detonation wave as in Ref. [29] and applied this pressure normal to all surfaces of the shell model throughout the entire simulation, even after extensive fracture and large deformation. Fluid-structure interaction effects were not modeled.

Here, we need to make a remark on the way we modeled the initial notch. The notches in the experiment were not machined through the entire depth of the shell. In this study, we modeled the notch by using the XFEM methodology, so we immediately allowed the translational and angular velocity fields across the notch to be discontinuous. The penalty part of the cohesive law in the compressive regime was activated to prevent incompatibilities in the compressive part (below the notch), but the tensile part of the cohesive law is not activated in the notch since the fracture in the notch is assumed to be completed. The penalty constants for these constraints did not affect the final results very much.

**5.1.1 Cylinder With Notch Size of  $L=5.08$  cm (Shot 7).** Figure 9 shows deformed configurations and contour plots of the effective plastic stress at the beginning of the backward crack propagation and just before and after the forward crack branches into two cracks. As we can see Fig. 9(c), the forward crack tip branches with an angle of 45 deg and forms stress concentrations ahead of two branched tips. In contrast to the forward moving branched tips, the backward tip retains its straight path.

Figure 10 shows the different perspective views of the computed deformed configurations at an intermediate stage at time  $t=256.86 \mu\text{s}$ . Subsequently, the forward branches turn to propa-

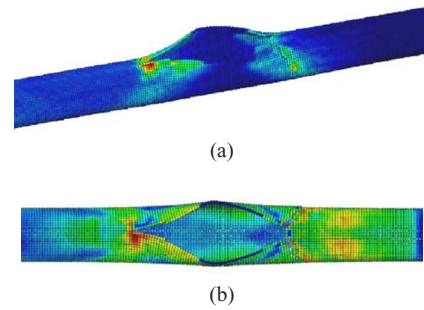


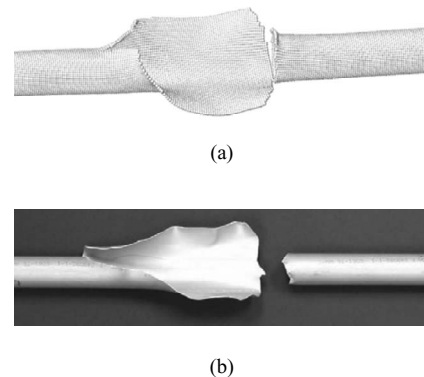
**Fig. 10 Evolution of crack opening at time  $t=256.86 \mu\text{s}$  along with distribution of effective plastic stress: (a) side view and (b) top view**

gate along the circumferential direction. The computed final configuration is shown in Fig. 11(a) along with the final experimental configuration, which is shown at Fig. 11(b). The computation reproduces some of the key features of the experiment quite well. In the computations, the crack propagates from the notch to the backward and the forward tips. The forward propagating crack then branches initially at 45 deg, but then turns to propagate along the axis of the cylinder. The experimental specimen shows evidence of similar crack branching and turning. As can be seen from Fig. 11(b), in the part of the pipe that has opened up, the crack progresses initially at an angle, but then the final crack path is circumferential, i.e., normal to the axis of the pipe. The computed crack paths are quite similar. In the center of the fracture, a little wedge shaped pipe is apparent. This is absent in the computation.

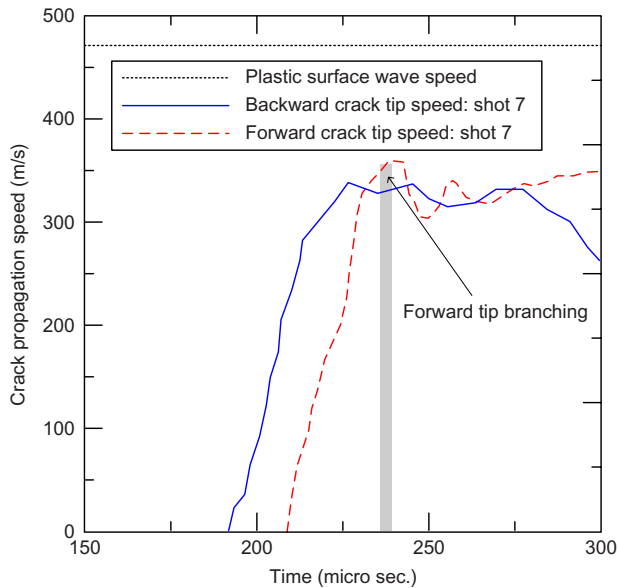
There are some discrepancies in the final configurations as can be seen from Fig. 11. The lower flap, as computed, opens up more than in the experiments. In the experiment, both the lower and the upper flaps show significant bends, but these are not apparent in the computation. This can be due to (1) absence of fluid-structure interaction effects in the computation, (2) errors in detonation wave loading function, particularly in the later stages, and (3) lack of fidelity in fracture criterion or material model.

Figure 12 shows time histories of the forward and backward crack propagation speeds. The forward crack tip starts to propagate around  $t=210.0 \mu\text{s}$  and then linearly speeds up and shows a peak speed around  $t=229.0 \mu\text{s}$ ; at this point the crack branches into two cracks. After branching, the crack tip loses speed, but then the speed recovers and reaches a plateau.

**5.1.2 Cylinder With Notch Size of  $L=2.54$  cm (Shot 4).** Experiments with the shorter notch showed substantially different crack evolution, and this is also evident in the computations. Figure 13 shows the distribution of effective plastic stress in the



**Fig. 11 Comparison of the final deformed shape between (a) the simulation result and (b) the experimental result (shot 7) [16,25]**



**Fig. 12** Comparison propagation speeds of two crack tips for the cylinder with the notch size of  $L=5.08$  cm (shot 7)

computed deformed configuration before the backward crack starts to rotate. As can be seen from Fig. 13(a), the axisymmetry of the stress field ahead of a backward crack tip is broken and then the crack tip path exhibits a change in direction as shown in Fig. 13(b). Note that this sudden direction change in crack path causes a concentration of plastic strain at the kinked points and it slows the crack speed as indicated in Fig. 14.

Figure 15 shows the different perspective views of the computed deformed configuration at time  $t=261.98 \mu\text{s}$ . As we can see from the figure, the backward crack turns to a circumferential path but the forward crack tip remains in a straight path. Shortly after this point, the strain concentration ahead of a forward crack tip is diffused and the crack tip is arrested.

A comparison between computational and experimental results of the final configuration is shown in Fig. 16. Again, the computed size of the crack opening in the pipe agrees reasonably well with the experiment and so do the crack paths, except that the transition from the axial path to a circumferential path is quite smooth in the computation, but rather rough in the experiment. The shapes of the flaps are not predicted well. Evidently, fluid-structure interaction effects play a substantial role in their shapes.

The computed crack propagation speeds for shot 7 and shot 4, which are shown in Figs. 12 and 14, respectively, are somewhat faster than the reported experimental crack speeds (maximum 250 m/s) [25]. This may be due to the shortcomings in the numerical representation of the crack, i.e., lack of crack tip blunting and tunneling phenomena in the numerical simulations.

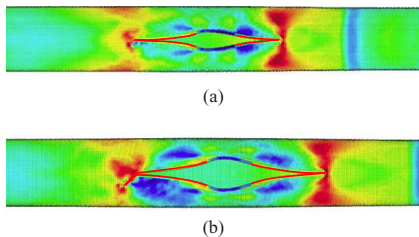


**Fig. 13** Evolution of crack and distributions of effective plastic stress at time times (a)  $t=231.41 \mu\text{s}$  and (b)  $t=239.05 \mu\text{s}$ . Note that finite element nodes are plotted and crack paths are explicitly marked.

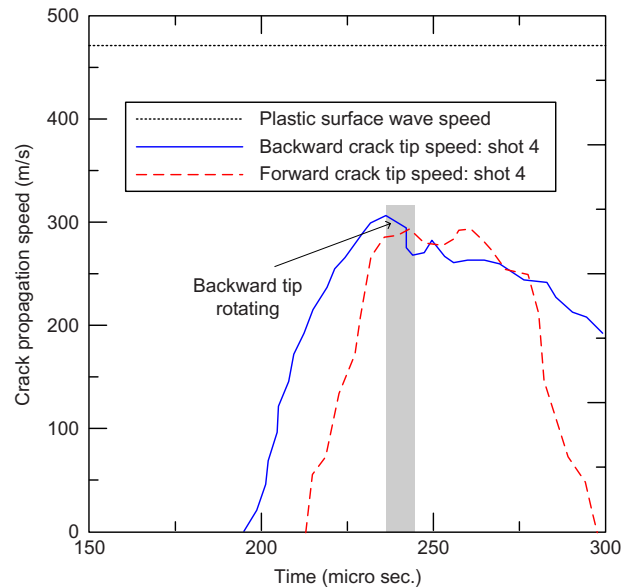


**Fig. 14** Comparison propagation speeds of two crack tips for the cylinder with the notch size of  $L=2.54$  cm (shot 4)

**5.2 Cylinder Fracture With an Initial Weak Spot.** We examine fracture patterns of the cylinder shown in Fig. 17(a). The cylinder is initially pressurized to 6.9 MPa ( $\approx 1000$  psi) and then the pressure at the center of the cylinder on a domain of radius  $r=2.50$  cm is increased until a fracture nucleates. We set an initial weak spot at two different locations as shown in Figs. 17(b) and 17(c), i.e., at the center of cylinder or close to the end cap.

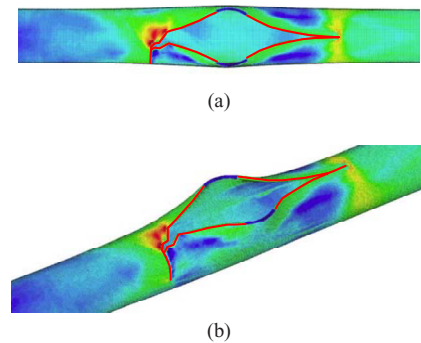


**Fig. 15** Evolution of crack and distributions of effective plastic stress at time  $t=261.98 \mu\text{s}$ : (a) top view and (b) side view

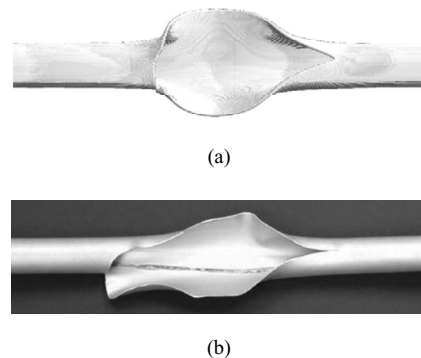


**Fig. 16** Comparison of the final deformed shape between (a) the simulation result and (b) the experimental result (shot 4) [16,25]

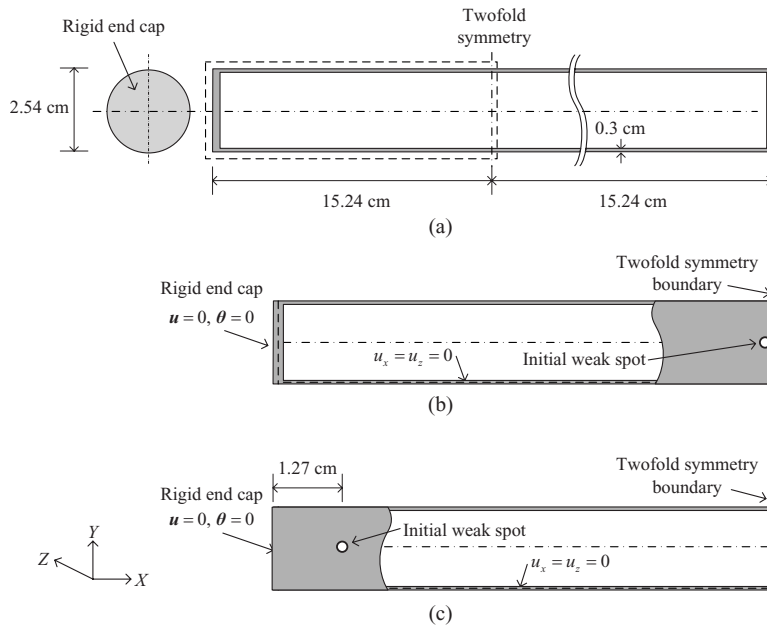


**Fig. 17 Setup for cylinder fracture with an initial weak spot: (a) only half of the cylinder is modeled due to the twofold symmetry, (b) cylinder with an initial weak spot at the center of the cylinder, and (c) cylinder with an initial weak spot close to the end cap**

Since the original cylinder, which has a length of 30.48 cm, has twofold symmetry, we modeled only half of the cylinder as shown in Figs. 17(b) and 17(c);  $u_x=0$  and  $\theta_x=\theta_y=\theta_z=0$  along the plane of twofold symmetry. This is somewhat unrealistic, but we just wish to demonstrate the ability to follow complicated crack paths. The model is discretized with a structured mesh of 8056 four-node quadrilateral shell elements. The rigid end cap is modeled by constraining all degrees of freedoms at the end cap. The material is aluminum 5086-H32, which has material properties: density  $\rho=2660.0 \text{ kg/m}^3$ , Young's modulus  $E=71.0 \text{ GPa}$ , Poisson's ratio  $\nu=0.30$ , and yield stress  $\sigma_y=207.0 \text{ MPa}$ . We used  $J_2$ -plasticity with a constant hardening slope  $h_p=634.0 \text{ MPa}$ . The fracture parameters are the same as in the previous example. The yield strength is reduced by 10% at the weak spots.

As we can see from Fig. 18, the crack initially forms at the weak spot and then propagates toward the end cap parallel to the axis of the cylinder. However, as the crack tip approaches the rigid end cap, the crack tip stress develops a strong shear component, which causes a sudden rotation of the crack trajectory.

The rigid end cap has a significant effect on the crack path. This can be observed by locating an initial weak spot near the rigid end cap as shown in Fig. 17(c). Under this setting, we originally anticipated development of three crack paths: two of them propagating toward the end cap after branching, and the other propagating toward the opposite end. However, only two crack tips are devel-

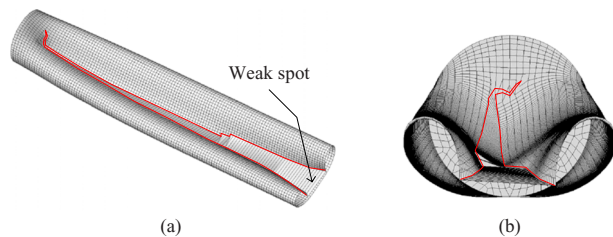


**Fig. 18 The computed final deformed shape along with marked opened crack surfaces: (a) perspective view and (b) axial view**

oped and propagate toward the end cap. This is due to the fact that the stored energy was only sufficient for two cracks, but it is not sufficient to develop a third crack toward the opposite side end. The deformed shape with crack opening is shown in Fig. 19. As we can see from Fig. 19, two cracks have propagated toward the end cap with the angle of 45 deg to the center line.

## 6 Conclusions

A method has been developed for the prediction of dynamic crack propagation in shells with explicit finite element methods. The methodology is based on the XFEM [1,2], but uses the Hansbo and Hansbo [3] implementation where the cracked element is treated by two superimposed elements with phantom nodes on the cracked portions [5,7].

A nonlocal fracture criterion based on the maximum tensile principal strain has been developed for a quasibrittle fracture where significant plastic deformation precedes fracture. In order to mitigate spurious predictions of fracture, the method uses a

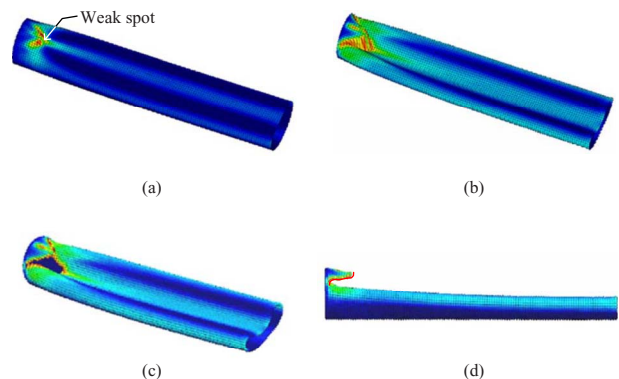


**Fig. 19 Evolution of crack opening and effective plastic strain distributions at different times: (a)  $t=187.0 \mu\text{s}$  and (b)  $t=252.0 \mu\text{s}$ . For a clear representation of crack opening, finite element nodes are plotted: (c) top view and (d) side view.**

weighted average of the strain ahead of the crack tip, i.e., a non-local strain. For the weighting function, a cubic spline that extends to approximately the edge of the near-tip plastic field was used.

In addition, a cohesive law was used across the crack surface. The cohesive law serves to represent plastic work and other fracture processes that are not resolved by the model.

Computations were made for two of the Chao and Shepherd [16] experiments of explosively loaded pipes. The finite element model was simply loaded by the pressure time history of the detonation traveling wave; fluid-structure interaction effects were not considered. Nevertheless, the computations reproduce many of the salient features of each experiment and differences in crack paths between two experiments.

For the pipe with the longer prenotch, the computations correctly predict crack branching at one end and the subsequent wrap-around of the crack path that severs the pipe at the other end. In the computation, the crack is arrested before the tube is completely severed, but there is some evidence (the notched piece in Fig. 11) that the complete breakage involved in the experiment a different loading. For the pipe with a shorter prenotch, a twisting of the crack path is correctly predicted. However, the deformed configurations observed experimentally show some deformations of the flaps of the pipe that are not replicated in the computation. These are probably due to fluid-structure effects that were not modeled.

Overall, these computational results show substantial promise for predicting the dynamic fracture behavior of explosively loaded shell structures. They furthermore indicate that in quasibrittle dynamic fracture, fracture criteria based on nonlocal strains are quite effective. It should be stressed that this observation probably only holds for relatively thin structure in quasibrittle materials such as aluminum, which exhibit fracture in tearinglike modes.

## Acknowledgment

The support of the Office of Naval Research under Grant Nos. N00014-06-1-0380 and N00014-06-1-0266 are gratefully acknowledged.

## References

- [1] Belytschko, T., and Black, T., 1999, "Elastic Crack Growth in Finite Elements With Minimal Remeshing," *Int. J. Numer. Methods Eng.*, **45**(5), pp. 601–620.
- [2] Moës, N., Dolbow, J., and Belytschko, T., 1999, "A Finite Element Method for Crack Growth Without Remeshing," *Int. J. Numer. Methods Eng.*, **46**(1), pp. 131–150.
- [3] Hansbo, A., and Hansbo, P., 2004, "A Finite Element Method for the Simulation of Strong and Weak Discontinuities in Solid Mechanics," *Comput. Methods Appl. Mech. Eng.*, **193**, pp. 3523–3540.
- [4] Mergheim, J., Kuhl, E., and Steinmann, P., 2005, "A Finite Element Method for the Computational Modelling of Cohesive Cracks," *Int. J. Numer. Methods Eng.*, **63**, pp. 276–289.
- [5] Song, J. H., Areias, P. M. A., and Belytschko, T., 2006, "A Method for Dynamic Crack and Shear Band Propagation With Phantom Nodes," *Int. J. Numer. Methods Eng.*, **67**, pp. 868–893.
- [6] Areias, P. M. A., Song, J. H., and Belytschko, T., 2005, "A Finite-Strain Quadrilateral Shell Element Based on Discrete Kirchhoff-Love Constraints," *Int. J. Numer. Methods Eng.*, **64**, pp. 1166–1206.
- [7] Areias, P. M. A., Song, J. H., and Belytschko, T., 2006, "Analysis of Fracture in Thin Shells by Overlapping Paired Elements," *Comput. Methods Appl. Mech. Eng.*, **195**, pp. 5343–5360.
- [8] Areias, P. M. A., and Belytschko, T., 2006, "A Comment on the Article: A Finite Element Method for Simulation of Strong and Weak Discontinuities in Solid Mechanics," *Comput. Methods Appl. Mech. Eng.*, **195**, pp. 275–276.
- [9] Belytschko, T., Chen, H., Xu, J., and Zi, G., 2003, "Dynamic Crack Propagation Based on Loss of Hyperbolicity With a New Discontinuous Enrichment," *Int. J. Numer. Methods Eng.*, **58**, pp. 1873–1905.
- [10] Réthoré, J., Gravouil, A., and Combescure, A., 2005, "An Energy-Conserving Scheme for Dynamic Crack Growth Using the Extended Finite Element Method," *Int. J. Numer. Methods Eng.*, **63**, pp. 631–659.
- [11] Elguedj, T., Gravouil, A., and Combescure, A., 2006, "Appropriate Extended Functions for X-Fem Simulation of Plastic Fracture Mechanics," *Comput. Methods Appl. Mech. Eng.*, **195**, pp. 501–515.
- [12] Cirak, F., Ortiz, M., and Pandolfi, A., 2005, "A Cohesive Approach to Thin-Shell Fracture and Fragmentation," *Comput. Methods Appl. Mech. Eng.*, **194**, pp. 2604–2618.
- [13] Areias, P. M. A., and Belytschko, T., 2005, "Nonlinear Analysis of Shells With Arbitrary Evolving Cracks Using XFEM," *Int. J. Numer. Methods Eng.*, **62**, pp. 384–415.
- [14] Ortiz, M., and Pandolfi, A., 1999, "Finite-Deformation Irreversible Cohesive Elements for Three-Dimensional Crack-Propagation Analysis," *Int. J. Numer. Methods Eng.*, **44**, pp. 1267–1282.
- [15] Armero, F., and Ehrlich, D., 2006, "Finite Element Methods for the Multi-Scale Modeling of Softening Hinge Lines in Plates at Failure," *Comput. Methods Appl. Mech. Eng.*, **195**, pp. 1283–1324.
- [16] Chao, T. W., and Shepherd, J. E., 2002, "Fracture Response of Externally-Flawed Cylindrical Shells to Internal Gaseous Detonation Loading," *Emerging Technologies in Fluids, Structures, and Fluid/Structure Interactions*, ASME Pressure Vessels and Piping Conference, Vancouver, BC, pp. 85–98.
- [17] Ahmad, S., Irons, B. B., and Zienkiewicz, O. C., 1970, "Analysis of Thick and Thin Shell Structures by Curved Finite Elements," *Int. J. Numer. Methods Eng.*, **2**, pp. 419–451.
- [18] Hughes, T. J. R., and Liu, W. K., 1981, "Nonlinear Finite Element Analysis of Shells: Part 2, Two dimensional Shells," *Comput. Methods Appl. Mech. Eng.*, **27**, pp. 167–181.
- [19] Hughes, T. J. R., and Liu, W. K., 1981, "Nonlinear Finite Element Analysis of Shells: Part 1, Three Dimensional Shells," *Comput. Methods Appl. Mech. Eng.*, **26**, pp. 331–362.
- [20] Belytschko, T., Lin, J. I., and Tsay, C. S., 1984, "Explicit Algorithms for the Nonlinear Dynamics of Shells," *Comput. Methods Appl. Mech. Eng.*, **42**, pp. 225–251.
- [21] Belytschko, T., Wong, B. L., and Chiang, H. Y., 1992, "Advances in One-Point Quadrature Shell Elements," *Comput. Methods Appl. Mech. Eng.*, **96**, pp. 93–107.
- [22] Belytschko, T., and Bachrach, W. E., 1986, "Efficient Implementation of Quadrilaterals With High Coarse-Mesh Accuracy," *Comput. Methods Appl. Mech. Eng.*, **54**, pp. 279–301.
- [23] Belytschko, T., and Leviathan, I., 1994, "Physical Stabilization of the 4-Node Shell Element With One Point Quadrature," *Comput. Methods Appl. Mech. Eng.*, **113**, pp. 321–350.
- [24] Papouliou, K. D., Sam, C. H., and Vavasis, S. A., 2003, "Time Continuity in Cohesive Finite Element Modeling," *Int. J. Numer. Methods Eng.*, **58**, pp. 679–701.
- [25] Chao, T. W., 2004, "Gaseous Detonation-Driven Fracture of Tubes," Ph.D. thesis, California Institute of Technology, Pasadena, CA.
- [26] Johnson, F. A., and Radon, J. C., 1975, "Evaluation of Fracture Energy of Aluminum Alloys," *J. Test. Eval.*, **3**, pp. 364–367.
- [27] Johnson, F. A., and Radon, J. C., 1976, "Fracture Energy and Crack Tunneling," *J. Test. Eval.*, **4**, pp. 209–217.
- [28] Roychowdhury, S., Roy, Y. D. A., and Dodds, R. H., Jr., 2002, "Ductile Tearing in Thin Aluminum Panels: Experiments and Analyses Using Large-Displacement, 3-D Surface Cohesive Elements," *Eng. Fract. Mech.*, **69**, pp. 983–1002.
- [29] Beltman, W. M., and Shepherd, J. E., 2002, "Linear Elastic Response of Tubes to Internal Detonation Loading," *J. Sound Vib.*, **252**, pp. 617–655.